Ice Pumping: Influence of Ice Thickness Gradients on the Arctic Ocean Circulation

GIANLUCA MENEGHELLO[a,b] AND MICHAEL A. SPALL[b]

[a] *Ecole normale supérieure, Université PSL, Paris, France*
[b] *Woods Hole Oceanographic Institution, Woods Hole, Massachusetts*

(Manuscript received 21 January 2026, in final form 5 May 2026, accepted 25 June 2026)

ABSTRACT: Surface currents beneath sea ice are influenced by ice thickness in much the same way bottom currents are influenced by bathymetry. Despite the gentle slope of the ice cover—only a few meters over thousands of kilometers—surface currents on the order of a few centimeters per second generate vertical velocities of a few meters per year, which are the same order of magnitude as the surface Ekman pumping. We dub this vertical velocity "ice pumping." Using theory and numerical modeling, we show that this ice pumping exerts a first-order control on both the structure and intensity of the large-scale Arctic Ocean circulation. We find that the dominant effect is the generation of a basin-scale anticyclonic circulation anomaly, forced by the interaction of the Transpolar Drift Current with the overlying sea ice that grows thicker toward Greenland. The most notable consequence is a shift of the Transpolar Drift Current itself toward the Eurasian coast and a modulation of the intensity of the large-scale circulation. Ice pumping should therefore be considered alongside Ekman pumping, mesoscale eddies, and the ice–ocean governor as a fundamental constraint on Arctic circulation and is likely to be important in other scenarios, such as underneath ice shelves and on ice-covered exoplanets.

KEYWORDS: Arctic; Sea ice; Ekman pumping/transport; Large-scale motions; Ocean dynamics; Gyres

1. Introduction

This paper examines how spatial variations in ice thickness can influence the large-scale circulation of the Arctic Ocean by inducing a vertical velocity at the ocean surface, which we refer to as "ice pumping."

In contrast to midlatitude basins, advection of planetary vorticity alone cannot balance the Ekman-driven vorticity input, as meridional gradients of planetary vorticity in the Arctic are too weak. A classical Sverdrup balance (Sverdrup 1947; Munk 1950) would therefore predict currents much stronger than observed, indicating the need for additional mechanisms. Three such mechanisms have been proposed.

The first is the advection of potential vorticity by the mean flow (Spall 2020) and by eddy fluxes (Davis et al. 2014; Lique et al. 2015; Manucharyan and Spall 2016; Yang et al. 2016; Meneghello et al. 2017). Advection by the mean flow matters when the forcing is asymmetric. Advection by eddy fluxes—generated by baroclinic instability—tends to relax the potential vorticity gradients generated by wind- and ice-driven Ekman pumping, and the flux divergence balances the vorticity input by the surface stress.

The second mechanism, dubbed the ice–ocean governor, involves the interaction between ice drift and surface currents (Meneghello et al. 2018a,b; Dewey et al. 2018; Zhong et al. 2018). As the surface-current velocity approaches the ice-drift velocity, surface stresses and Ekman pumping weaken, leading to a substantial reduction in potential vorticity input and, consequently, a reduced need for potential vorticity advection. Subsequent theoretical (Doddridge et al. 2019) and observational (Meneghello et al. 2020) studies have shown that both mean/eddy advection and the ice–ocean governor contribute to the equilibration of the Arctic circulation, albeit on different time scales.

A third mechanism influencing the large-scale circulation in high-latitude oceans is the interaction between currents and bathymetry. In the absence of strong planetary vorticity gradients, the barotropic component of the flow tends to follow bathymetric contours to conserve potential vorticity. Although this steering weakens as the flow becomes more baroclinic over long time scales, bathymetry can still influence long-term mean currents (Nöst and Isachsen 2003), and remotely forced deep flows may exert a similar steering effect on the surface circulation (Nilsson et al. 2024). In the present work, however, we focus on mechanisms that operate in the surface circulation, away from coastlines and independently of topographic control, and therefore neglect bathymetric effects.

The ice pumping mechanism introduced here represents a fourth contribution. In this framework, summarized in Fig. 1, ice thickness acts as an upside-down bathymetry and steers the currents away from the pathways they would otherwise follow in the absence of ice thickness gradients. Although ice thickness gradients are two to three orders of magnitude smaller than bathymetric ones, surface currents are much stronger than their deep counterparts and are subject to forcing by surface stresses, making the current/ice slope interaction nonnegligible. Importantly, this upside-down bathymetry interacts with both barotropic and baroclinic components and therefore remains relevant even on the long time scales over which deep currents are expected to be weak.

Our discussion is organized as follows. Section 2 introduces a dynamical balance that includes Ekman pumping, the advection of planetary vorticity, eddy fluxes, the ice–ocean governor, and the ice pumping associated with the upside-down bathymetry. We provide observational and theoretical estimates of the role played by each process. We focus on the

Corresponding author: Gianluca Meneghello, gianluca.meneghello@lmd.ipsl.fr

DOI: 10.1175/JPO-D-26-0022.1

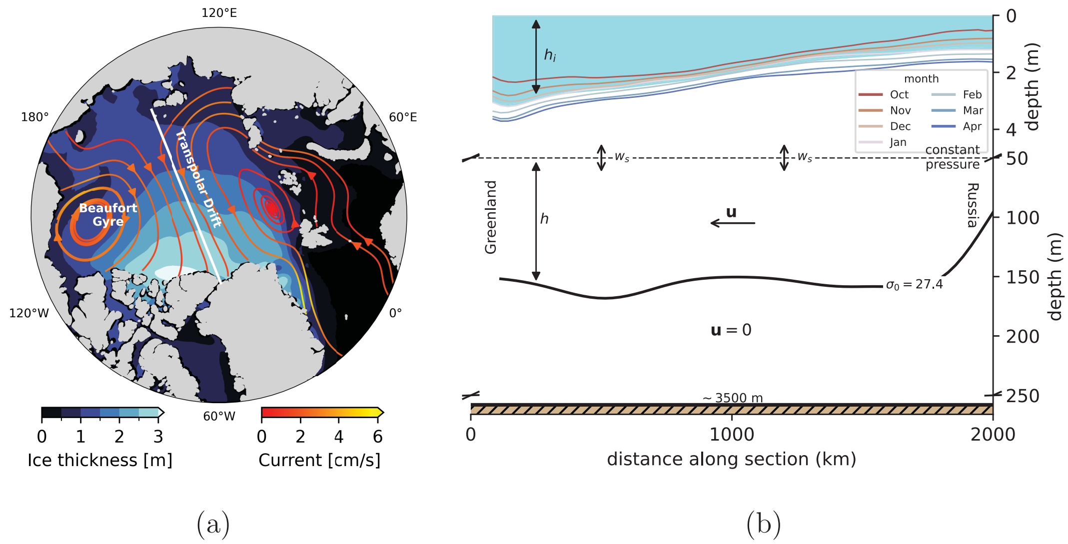

FIG. 1. (a) Ocean currents (streamlines) flowing beneath a sloped sea ice cover (contours) induce an ice-pumping effect analogous to Ekman pumping, locally squeezing or stretching the underlying water column. (b) Schematic representation of ice pumping, illustrating the conceptual model used in this study based on observations along the white line in (a). Ocean currents in (a) are computed from dynamic ocean topography (Armitage et al. 2016, 2017), sea ice thickness in both panels is from Ricker et al. (2017), while the isopycnal depth in (b) is from the *World Ocean Atlas*. Datasets are restricted to the cold-season period (15 Oct–15 Apr) and averaged over 2011–20, reflecting the availability of sea ice thickness observations.

equilibrated state, assume that deep currents are at rest, and use a simple thickness-diffusion parameterization to represent mesoscale and submesoscale processes. We relax several of these assumptions in section 3, where we examine the role of ice pumping using a shallow-water numerical model. Such a model allows us to include a nonparameterized eddy field, barotropic and first baroclinic modes, and a time-varying forcing. We conclude in section 4 with a discussion of the implications for the Arctic circulation in particular and for ice-covered oceans more generally.

2. The role of ice pumping in driving the large-scale circulation

a. *Dynamical balance*

Our analysis starts with the geostrophic relations and the vertically integrated continuity equation (including an eddy thickness flux divergence) for the 1.5-layer model shown in Fig. 1b:

$$u = -\frac{g'}{f}\frac{\partial h}{\partial y} \qquad v = \frac{g'}{f}\frac{\partial h}{\partial x}, \tag{1a}$$

$$\nabla\cdot(\mathbf{u}h + \overline{\mathbf{u}'h'}) = -w_s, \tag{1b}$$

where h is the layer thickness, $\mathbf{u} = (u, v)$ is the time-averaged geostrophic velocity, $\overline{\mathbf{u}'h'}$ is the thickness flux due to eddies, g' is the reduced gravity, and w_s is the vertical velocity at a constant pressure depth below the well-mixed surface layer and is defined as positive upward (upwelling) as in Fig. 2. We here neglect the bathymetry-induced vertical velocity at the ocean floor, consistently with the assumption that the bottom layer is at rest. We also assume that the flow is adiabatic so there is no mass exchange between the upper layer and the deep layer. A constant layer thickness h_b is imposed as a boundary condition to enforce no normal flow.

Substitution of the geostrophic relations into the continuity equation, and assuming a simple parameterization of mesoscale and submesoscale thickness fluxes $\overline{\mathbf{u}'h'} = -K\nabla h$ with K being a constant diffusivity, we obtain

$$\underbrace{\frac{g'}{2f^2}J(f,h^2)}_{\text{planetary vorticity advection}} - \underbrace{K\nabla^2 h}_{\text{thickness diffusion}} = -w_s. \tag{2}$$

The first term represents ageostrophic divergence due to the advection of planetary vorticity, and the second term is the parameterized thickness diffusion. $J(a, b) = (\hat{\mathbf{k}}\times\nabla a)\cdot\nabla b = [(\partial a/\partial x)(\partial b/\partial y)] - [(\partial a/\partial y)(\partial b/\partial x)]$ is the Jacobian.

The vertical velocity w_s includes both an Ekman pumping component and an ice pumping component, the latter driven by currents flowing under the sloping sea ice cover,

$$w_s = \underbrace{\nabla\times\frac{\boldsymbol{\tau}}{\rho f}}_{\text{Ekman pumping}} - \underbrace{\mathbf{u}\cdot\nabla h_i}_{\text{ice pumping}}, \tag{3}$$

where $\boldsymbol{\tau}$ is the stress at the ocean surface and ∇h_i is the ice thickness gradient. This formulation is analogous to that of Ekman pumping over uneven terrain but applied here to a

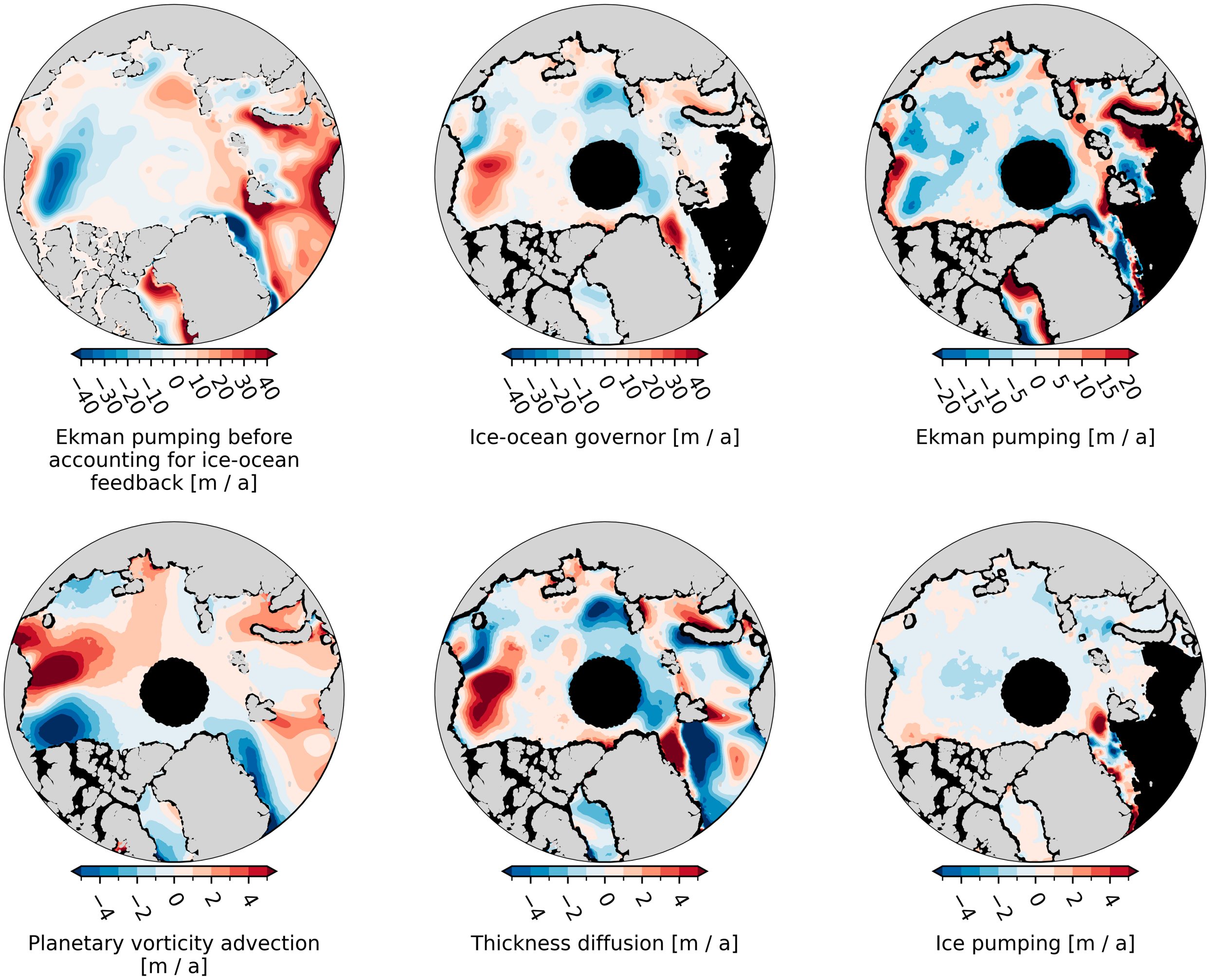

FIG. 2. Observational estimates of the individual contributions to the vorticity balance, as defined in Eq. (4) (m a^{-1}). The values of the parameters are taken from Table 1. The observational datasets used in this estimate are sea ice thickness from Ricker et al. (2017), sea ice concentration from Meier et al. (2024), sea ice velocity from Tschudi et al. (2019), dynamic ocean topography from Armitage et al. (2016, 2017), and geostrophic winds derived from atmospheric geopotential fields from Hersbach et al. (2023). To focus on the variability in the central Arctic, the color scale in the bottom three panels is saturated at 65 m a^{-1}. Datasets are restricted to the cold-season period (15 Oct–15 Apr) and averaged over 2011–20, reflecting the availability of sea ice thickness observations.

surface Ekman layer—see, e.g., Cushman-Roisin and Beckers (2010, sections 8.5 and 8.6). Ice pumping is negative (downwelling) if the velocity is in the direction of the ice thickness gradient, as in Fig. 1.

We assume that the thickness gradient ∇h_i remains constant in time. This approximation significantly simplifies the analysis and is supported by observational estimates of ice thickness (color lines in Fig. 1b), which show that although the total thickness varies, its slope remains largely stable across seasons. This assumption is also supported by theoretical considerations. A small ice thickness gradient, on the order of 10^{-6}, combined with an ice velocity of a few centimeters per second, implies a vertical velocity at the ice–ocean interface of only a few millimeters per day, well within typical ice growth rates. Ice production can readily balance the divergence of ice thickness flux. In addition, numerical calculations in the following section show that the system is essentially linear in time such that the mean circulation with a time-dependent ice slope is the same as the steady circulation with the mean ice slope.

Furthermore, we assume a continuous sea ice concentration field, as is commonly done in large-scale sea ice models. We consider ice pumping to be effective primarily when the sea ice concentration exceeds approximately 80%. At lower concentrations, the ice is generally in free drift and has a negligible large-scale thickness gradient; as a result, the ocean circulation will not be significantly influenced by the ice surface slope.

Under the additional, and more common, assumptions that (i) the surface stress is linear in the wind and ice–ocean relative velocity, $\boldsymbol{\tau} = (1-\alpha)C_a\rho_a\mathbf{u}_a + \alpha C_i\rho(\mathbf{u}_i - \mathbf{u})$, where α is the ice concentration; (ii) gradients of the ice concentrations are negligible in the Ekman pumping computations,

TABLE 1. Parameters and Arctic reference values.

Symbol	Expression	Value	Units	Description
f_0	—	1.45×10^{-4}	$\mathrm{s^{-1}}$	Coriolis parameter
β_0	—	0	$\mathrm{m^{-1}\,s^{-1}}$	Meridional gradient of Coriolis parameter
a	—	6.4×10^{6}	m	Earth's radius
γ_0	f_0/a^2	3.5×10^{-18}	$\mathrm{m^{-2}\,s^{-1}}$	Second derivative of the Coriolis parameter (γ-plane approximation)
H	—	100	m	Characteristic layer thickness anomaly
H_i	—	1	m	Characteristic ice thickness anomaly
L	—	1×10^{6}	m	Characteristic horizontal length
K	—	300	$\mathrm{m^2\,s^{-1}}$	Eddy diffusivity
C_i	—	5×10^{-4}	$\mathrm{m\,s^{-1}}$	Drag velocity (dimensional)
U_i	—	2×10^{-2}	$\mathrm{m\,s^{-1}}$	Ice velocity
g'	$\frac{g\Delta\rho}{\rho}$	2.5×10^{-2}	$\mathrm{m\,s^{-2}}$	Reduced-gravity
U	$\frac{g'}{f_0}\frac{H}{L}$	2×10^{-2}	$\mathrm{m\,s^{-1}}$	Geostrophic velocity
W	$\frac{C_i}{f_0}\frac{U_i}{L}$	1×10^{-7}	$\mathrm{m\,s^{-1}}$	Ekman pumping velocity
B	$\frac{U}{W}\frac{H}{L}\frac{\gamma_0 L^2}{2f_0}$	0.30	—	Nondimensional planetary vorticity parameter
G	$\frac{U}{W}\frac{C_i}{f_0 L}$	0.86	—	Nondimensional ice–ocean governor parameter
P	$\frac{U}{W}\frac{H_i}{L}$	0.25	—	Nondimensional ice-pumping parameter
K	$\frac{K}{W}\frac{H}{L^2}$	0.43	—	Nondimensional eddy diffusivity parameter

$\nabla \times (\alpha \mathbf{u}) \approx \alpha \nabla \times \mathbf{u}$; (iii) variations of the Coriolis parameter f are negligible in all terms except the planetary vorticity advection; and (iv) $\mathbf{u}$ is the geostrophic velocity given by (1a), so that vorticity can be expressed as $\nabla \times \mathbf{u} = (g'/f_0)\nabla^2 h$, the dynamical balance [(2)] can be formulated in terms of the layer thickness h:

$$\underbrace{\frac{g'}{2f_0^2}J(f,h^2)}_{\text{planetary vorticity advection}} - \underbrace{K\nabla^2 h}_{\text{thickness diffusion}} = \underbrace{-[(1-\alpha)w_a + \alpha w_i]}_{\text{Ekman pumping before accounting for ice-ocean feedback}} + \underbrace{\alpha\frac{C_i g'}{f_0^2}\nabla^2 h}_{\text{ice-ocean governor}} + \underbrace{\frac{g'}{f_0}J(h,h_i)}_{\text{ice pumping}}, \tag{4}$$

where $w_a = (C_a/f_0)(\rho_a/\rho)\nabla \times \mathbf{u}_a$ and $w_i = (C_i/f_0)\nabla \times \mathbf{u}_i$ are the prescribed wind- and ice-driven Ekman pumpings before accounting for any ice–ocean feedback and $(C_i g'/f_0^2)\nabla^2 h = (C_i/f_0)\nabla \times \mathbf{u}$ is the feedback of the ocean currents flowing below sea ice on the ice-driven Ekman pumping, which is commonly referred to as the ice–ocean governor and is here interpreted as an equivalent Ekman pumping partially reducing w_i. The last term on the right-hand side $(g'/f_0)J(h, h_i) = \mathbf{u}\cdot\nabla h_i$ represents the effect of ice pumping.

It is worth noting that, under the β-plane approximation, the first term on the left-hand side reduces to the classical Sverdrup term $[g'\beta_0/(2f_0^2)](\partial h^2/\partial x)$. In polar regions, however, the β-plane approximation does not hold, and a higher-order expansion of the gradient of the Coriolis parameter is required:

$$f(s) \approx f_0 + \beta_0 s + \frac{\gamma_0}{2}s^2, \tag{5}$$

where $\beta_0 = \partial f/\partial s$, $\gamma_0 = \partial^2 f/\partial s^2$, and $s = \sqrt{x^2 + y^2}$ is the distance from the North Pole.

b. Dimensional analysis

Insights into the role of the different processes in the balance [(4)] can be obtained by making the equation dimensionless after defining a characteristic vertical length scale H, horizontal length scale L, geostrophic velocity scale U, and an Ekman pumping scale W. We furthermore denote the characteristic ice thickness scale as H_i. Note that these choices reflect basin-scale balances, not smaller-scale gyres or boundary currents. The dimensionless balance can be rewritten as

$$\underbrace{B\tilde{J}(\tilde{f},\tilde{h}^2)}_{\text{planetary vorticity advection}} - \underbrace{(\alpha G + K)\tilde{\nabla}^2\tilde{h}}_{\text{ice-ocean governor and thickness diffusion}} - \underbrace{P\tilde{J}(\tilde{h},\tilde{h}_i)}_{\text{ice pumping}} = \underbrace{-[(1-\alpha)\tilde{w}_a + \alpha\tilde{w}_i]}_{\text{Ekman pumping before accounting for ice-ocean feedback}}. \tag{6}$$

The dimensionless parameters B, K, G, and P, defined in Table 1, quantify the relative roles of planetary vorticity advection, eddy fluxes, ice–ocean coupling, and ice pumping. In the Arctic, all of them take characteristic values of order 1. The right-hand side involves only the prescribed Ekman pumping terms $\tilde{w}_a = w_a/W$ and $\tilde{w}_i = w_i/W$ weighted by the

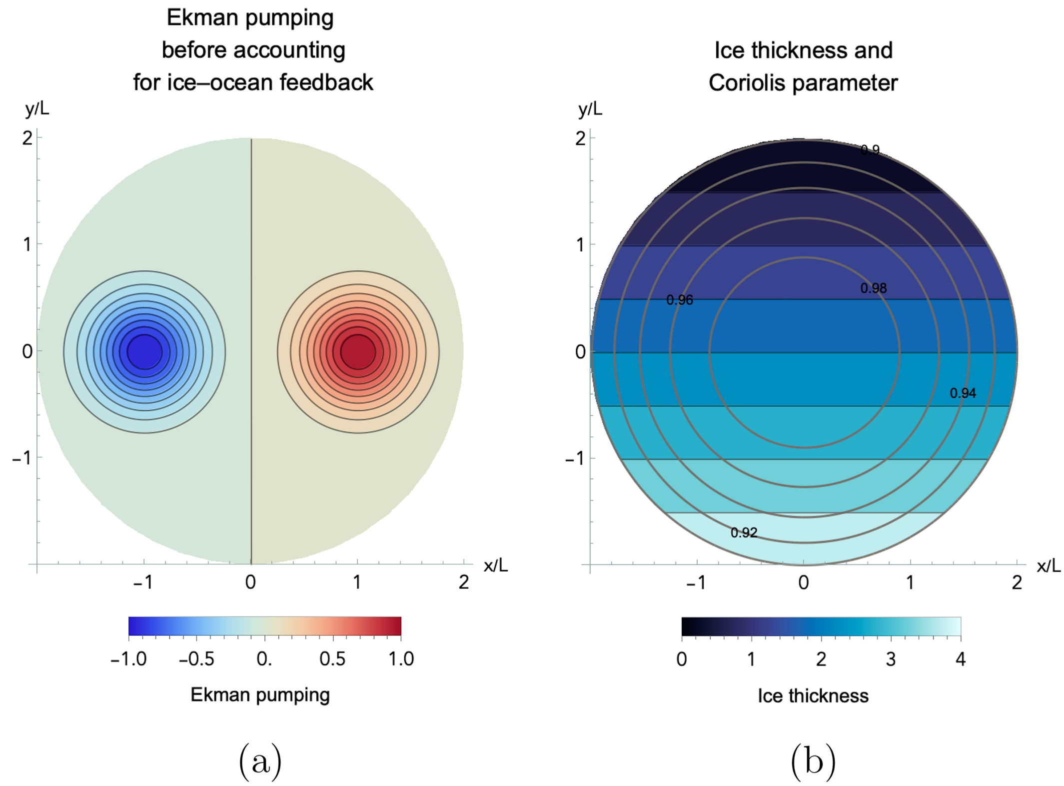

FIG. 3. The model setup. (a) Ekman pumping prior to the inclusion of ice–ocean feedback; (b) ice thickness (color) and dimensionless Coriolis parameter f/f_0 (contours).

ice concentration α and nondimensionalized by the velocity scale W. Tildes denote dimensionless variables and operators, and $\tilde{f} = f/f_0$.

Observational estimates for each of these terms are shown in Fig. 2 to demonstrate their approximate magnitudes and patterns. The Ekman pumping is largest in the Beaufort Gyre because of the anticyclonic wind stress curl arising from the Beaufort high. The ice–ocean governor term is nearly as large and of opposite sign because the ice motion spins up the ocean currents, thus reducing the differential velocity $\mathbf{u}_i - \mathbf{u}$ upon which the surface stress depends, so that the effective Ekman pumping is much weaker than would be if the ocean currents were neglected. Planetary vorticity advection is large, and probably larger than commonly assumed, in the Beaufort Gyre, reflecting the strong anticyclonic circulation there. Thickness diffusion is upward in the gyre region as a result of the export of low potential vorticity eddies from the gyre and is weak over much of the central Arctic. Ice pumping is smaller than the other terms along the coastlines but comparable in magnitude and consistently negative in the entire Arctic interior, indicating its importance for the large-scale circulation.

It is worth remarking that both the eddy fluxes and the ice–ocean governor parameters, K and G, multiply a Laplacian, despite representing very different physical processes: a parameterized thickness diffusion by mesoscale turbulence for eddy fluxes and the vorticity of the surface geostrophic current for the ice–ocean governor.

c. Dynamical balances of the Arctic Ocean circulation

To understand the interplay among the different processes, it is instructive to solve the dynamical balance [(6)] under several different limits. We start by separately investigating the balance between Ekman pumping and (i) planetary vorticity advection, (ii) governor/eddy fluxes, and (iii) ice pumping. The other terms for each configuration are deactivated by setting the corresponding parameter to zero, with the exception of the eddy fluxes and the ice–ocean governor parameters that are set to a minimum of $\alpha G + K = 10^{-3}$ solely for numerical stability. The imposed Ekman-pumping field, ice thickness, and Coriolis parameter distribution, common to all configurations, are shown in Fig. 3.

A Dirichlet boundary condition $\tilde{h}_b = 3$, where $\tilde{h}_b$ denotes the dimensionless layer thickness at the boundary, is imposed along the basin perimeter, thereby enforcing zero normal mean flow. A nonzero boundary thickness flux may nonetheless arise from eddy transport, $\overline{\mathbf{u}'h'} \approx -K\nabla h$, and the domain boundary is assumed to lie outside any boundary layer developing near the coastline or continental shelves and redistributing any thickness flux arising from this eddy transport. It is worth remarking that the specific value of the boundary condition affects only the weight of the nonlinear planetary vorticity advection term, as can be seen by linearizing about $\tilde{h} = \tilde{h}_b + \tilde{h}'$, which yields $J(\tilde{f}, \tilde{h}^2) \approx 2\tilde{h}_b J(\tilde{f}, \tilde{h}')$.

The resulting circulations, as inferred from the layer thickness (streamfunction), are shown in Fig. 4. Potential vorticity

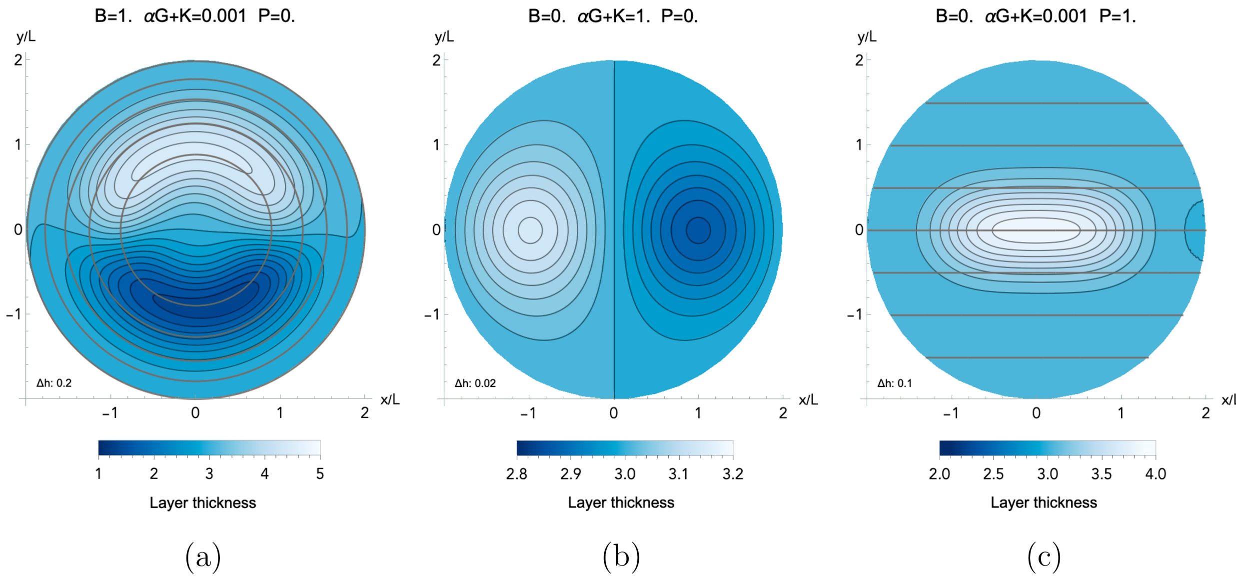

FIG. 4. (a) The planetary-vorticity-balanced circulation—equivalent to the Sverdrup balance at lower latitudes; (b) the governor/thickness-diffusion-balanced circulation; (c) the ice-pumping-balanced circulation. Gray contours mark lines of constant Coriolis parameter in (a) and constant ice thickness in (c), the same as in Fig. 3b. Contour spacing and color bars differ among panels.

conservation governs the circulation in all cases, but the computed currents differ both in direction and magnitude. When planetary vorticity advection is the sole balance to Ekman pumping, as in Fig. 4a, flow outside the Ekman-pumping region follows f contours, marked by gray circles. Within the Ekman-pumping region, upwelling stretches the water column and drives flow poleward—toward larger f, conserving f/h—while downwelling compresses the column and drives flow equatorward toward smaller f. Potential vorticity is advected solely by the mean flow, which is confined to narrow, intense currents near the pole. Counterintuitively, the Transpolar Drift Current flows from the upwelling region on the right toward the downwelling region on the left (see Fig. 3a), and the extrema in layer thickness occur where the Ekman pumping is zero rather than near the regions of maximum upwelling and downwelling. The planetary-vorticity-balanced flow is nearly perpendicular to the observed Arctic circulation, highlighting the importance of the remaining terms. A similar circulation pattern was found by Willmott and Luneva (2015) for a barotropic polar plane.

The eddy- and ice-ocean-governor-balanced circulation is shown in Fig. 4b. Eddies flux potential vorticity between the downwelling region and the upwelling region, and from the gyres toward the boundaries, and the mean flow merely reflects the requirement for an isopycnal slope to sustain these eddy fluxes. In contrast, the ice–ocean governor reduces the Ekman pumping, and the mean flow reflects the surface currents catching up with the ice drift and limiting the surface stress. In both regimes, the mean flow does not transport net potential vorticity between upwelling and downwelling regions, and the flow is substantially weaker. Two counterrotating gyres develop, matching the imposed Ekman pumping pattern and canceling its effect.

Last, the ice-pumping-balanced circulation is shown in Fig. 4c. Outside Ekman-pumping regions, the current is forced to follow ice thickness contours, marked by gray horizontal lines, to conserve potential vorticity and is thus blocked when these intersect the boundary. Within the forcing region, Ekman upwelling drives the circulation toward thicker ice at the bottom of the figure, generating a compensating ice-pumping downwelling, and vice versa. The combined effect is a single anticyclonic gyre spanning the entire area between the two Ekman pumping regions. This solution is analogous to the response to Ekman forcing on a midlatitude β plane, with the ice thickness gradient taking the role of β. As is the case for the ice–ocean governor, the current flowing beneath the sloping sea ice cover cancels the Ekman pumping. The net transport of potential vorticity between the upwelling and downwelling regions is zero, as can be inferred from the streamfunction being parallel to the ice thickness contours.

How does ice pumping reshape the circulation when all processes contribute to the balance? Figure 5 shows the circulation when planetary vorticity advection and governor/eddy fluxes, but no ice pumping, are active ($B = 1$, $\alpha G + K = 1$, $P = 0$) (Fig. 5a) and when all three processes are active ($B = 1$, $\alpha G + K = 1$, $P = 1$) (Fig. 5b). The introduction of the ice pumping modifies the circulation by shifting and deflecting the Transpolar Drift Current toward the Eurasian coast on the right. Its net effect, shown in Fig. 5c, is an anticyclonic circulation whose transport per unit depth $\tilde{T} = \max(\tilde{h}) - \tilde{h}_b \approx 0.1$ is comparable to the $\tilde{T} \approx 0.2$ transport of the two original gyres.

3. Numerical experiments

The basic influences of ice cover slopes predicted by the theory in section 2 are now evaluated with the use of an idealized

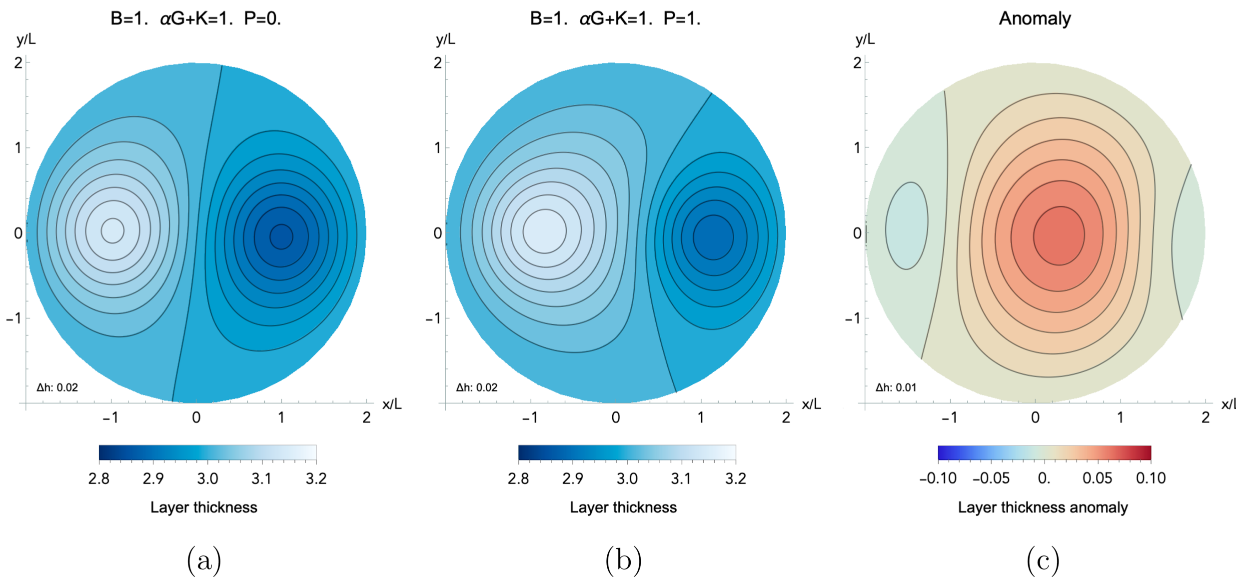

FIG. 5. The circulation (a) without and (b) with ice pumping. Planetary vorticity advection and eddy-flux/ice–ocean governor are given equal weight. (c) The introduction of ice pumping generates an anomalous circulation between the two gyres driving a cross-gyre transport comparable to the transport of the original gyre.

numerical model. The model solves the two-layer shallow water equations in a circular domain with a pole at its center. The model is forced by a specified surface stress representing the stress imparted on the ocean by either wind or ice motion, before accounting for ice–ocean feedback. The model includes physics not represented in the theory, including nonlinearities, explicit eddy fluxes, two active layers, and explicit closure of eddy fluxes at the boundaries. The influence of ice pumping is demonstrated by adding a vertical velocity $\mathbf{u}_1 \cdot \nabla h_i$ to the continuity equation of layer 1 to represent the pumping/suction resulting from surface currents oriented along the ice cover slope.

a. Model formulation

The momentum equations are written as

$$\frac{\partial u_k}{\partial t} + (f + \zeta_k)v_k = -\frac{\partial(P_k + E_k)}{\partial x} - \delta_{k1}\frac{C_i u_k}{h_k} - \delta_{k2}\frac{C_d u_k}{h_k} + A\nabla^2 u_k, \tag{7a}$$

$$\frac{\partial v_k}{\partial t} - (f + \zeta_k)u_k = -\frac{\partial(P_k + E_k)}{\partial y} + \delta_{k1}\frac{\tau^y}{\rho_0 h_k} - \delta_{k1}\frac{C_i v_k}{h_k} - \delta_{k2}\frac{C_d v_k}{h_k} + A\nabla^2 v_k, \tag{7b}$$

where $k = 1, 2$ is the layer; u and v are the horizontal velocities in the x and y directions, respectively; h is the layer thickness; τ^y is the stress in the y direction; $\zeta_k = \partial/\partial x - \partial u_k/\partial y$ is the relative vorticity; P_k is the pressure; $E_k = (u_k^2 + v_k^2)/2$ is the kinetic energy; $g' = (\rho_2 - \rho_1)g/\rho_2$ is the reduced gravity; and ρ_0 is a reference density. The δ_{ij} is the Kroneker delta, which equals one when $i = j$ and zero otherwise. The Coriolis parameter varies with latitude as $f = 1.45 \times 10^{-4}\sin\theta$, where θ is the latitude with the pole at the center of the domain. The model is forced by a stress in the y direction applied as a body force in layer 1. Dissipation is represented by a linear bottom drag in layer 2 (C_d), a linear ice–ocean drag in layer 1 (C_i), and a lateral Laplacian viscosity with no-slip boundary conditions. The viscosity coefficient A is dependent on the velocity strain and shear, following Smagorinsky (1963), as

$$A = (\nu_s/\pi)^2\Delta^2\left[\left(\frac{\partial u}{\partial x} - \frac{\partial v}{\partial y}\right)^2 + \left(\frac{\partial u}{\partial y} + \frac{\partial v}{\partial x}\right)^2\right]^{1/2}, \tag{8}$$

where ν_s is the dimensionless Smagorinsky coefficient and Δ is the grid spacing.

There is no exchange of mass between layers in the continuity equation, but there is a mass source term forced by the gradient in ice thickness added at the top of layer 1:

$$\frac{\partial h_k}{\partial t} + \nabla\cdot(h_k\mathbf{u}_k) = -(2 - k)\mathbf{u}_1\cdot\nabla h_i. \tag{9}$$

The term on the right-hand side is the vertical velocity resulting from the horizontal velocity interacting with the ice cover slope (only applied to layer 1). In this construct, we can think of the surface of layer 1 as residing at the base of the ice at its thickest point. The vertical velocity through this surface represents the conservation of mass in the region between the ice and this surface. The top of layer 1 is also a surface of uniform pressure arising from the ice and water lying above it, so in that sense it is akin to a free surface in the absence of sea ice.

This formulation differs slightly from the theory derived in section 2, which assumes that the velocity at the ice–ocean

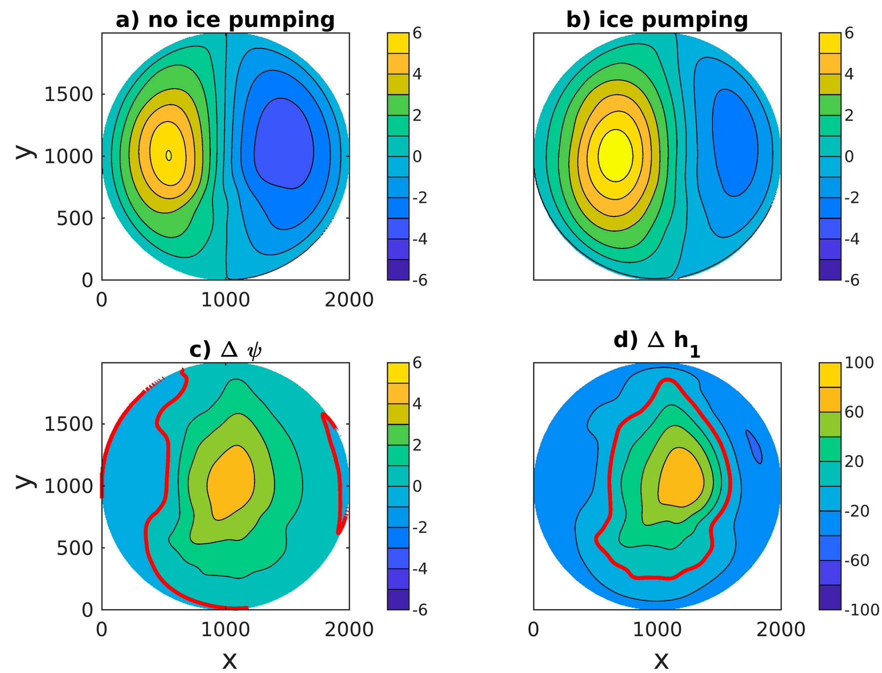

FIG. 6. Upper-layer streamfunction (Sv) for the case with ice–ocean drag but (a) no ice pumping and (b) with ice pumping. The difference between the case with ice pumping relative to the case without ice pumping for the upper-layer (c) streamfunction (Sv) and (d) thickness (m). The red line in (c) and (d) is the zero contour.

interface is given by the geostrophic flow, while the primitive equation model derives the ice pumping from the full velocity field, including contributions from ageostrophic flows. To leading order, we expect the large-scale halocline flow to be in geostrophic balance but recognize that, on small scales, the ageostrophic terms may become important.

Finally, the pressure is calculated from the hydrostatic equation as

$$P_1 = g(h_1 + h_2), \qquad P_2 = P_1 - g'h_1. \tag{10}$$

The model domain is circular with radius $r_0 = 1000$ km and a flat bottom. The initial layer thicknesses are $h_1 = 200$ m and $h_2 = 400$ m with a reduced-gravity between the two layers of $g' = 0.025$ m s^{-2}. The horizontal grid spacing is 5.5 km, which is less than the baroclinic deformation radius of 13 km, so the model resolves first-mode baroclinic eddies well. The surface stress is independent of y and defined to represent two gyres separated by a flow in the negative y direction. This is a crude representation of the anticyclonic Canada Basin and cyclonic Eurasian Basin, separated by the Transpolar Drift Current directed from Russia toward Greenland (see Fig. 1). The maximum surface stress is $\tau_0 = -0.015$ N m^{-2}, and its spatial pattern is given by

$$\tau^y = \tau_0 \cos[\pi(x - r_0)/r_0]. \tag{11}$$

The depth of the sea ice is specified as a linear function of y, increasing from $h_{\min} = 0.5$ m at $y = 2r_0$ km to $h_{\max} = 5.5$ m at $y = 0$:

$$h_i = h_{\min} + (h_{\max} - h_{\min})(2r_0 - y)[1 + \phi\cos(2\pi t/\Theta)]/(1 + \phi). \tag{12}$$

This is, of course, a gross simplification of the actual ice distribution, which varies in space and time. The term proportional to ϕ represents a simple seasonal cycle, where Θ is 1 year, although for our central calculation $\phi = 0$. The model does not have an active ice component, and the ice is not advected by the ocean. We assume that the ice distribution is a steady balance between wind stress, ocean stress, internal ice stresses, and formation/melt from interactions with the atmosphere and ocean. This is justified by the observation that ice is present near Greenland at all times and, over long space and time scales, follows a general pattern of increasing ice thickness in the direction of Greenland. A simple model for the ice thickness in the central Arctic demonstrates such a steady balance (Spall 2019).

For the central calculation, the model was run for a period of 40 years with mean fields calculated over the final 15 years of integration. The bottom drag coefficient is $C_d = 0.0012$ m s^{-1}, and the ice–ocean drag coefficient is $C_i = 1 \times 10^{-4}$ m s^{-1}. The nondimensional Smagorinsky Laplacian coefficient is $\nu_s = 2.5$. The primary sensitivity to these choices is that the gyres become more unstable for lower values of C_i, resulting in weaker mean gyres (Meneghello et al. 2020, 2021).

The ice–ocean drag coefficient is smaller than the bottom-drag coefficient and the scaling value in Table 1. This weaker drag allows halocline-depth mesoscale eddies to develop in the model, as are observed. This weaker drag is required

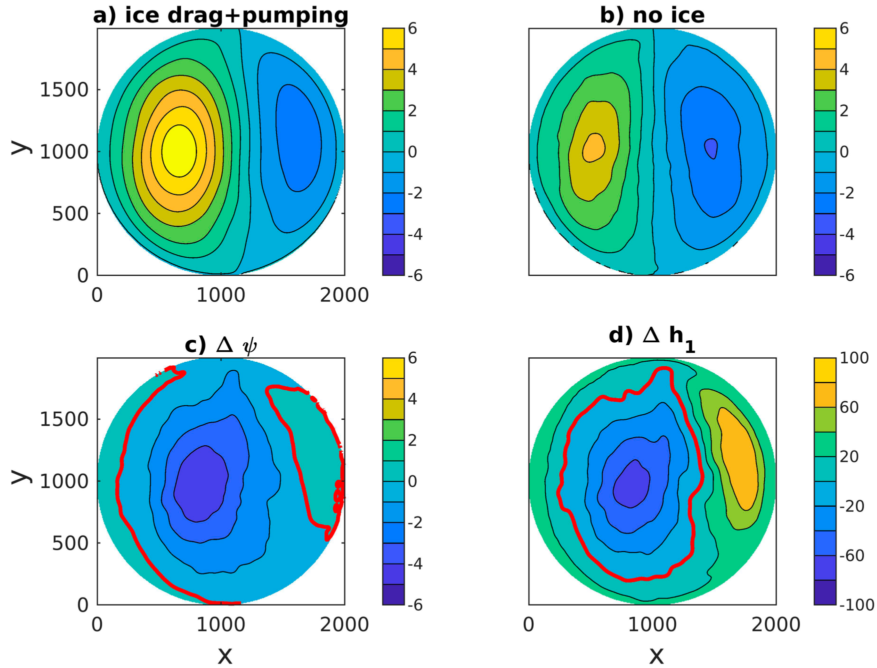

FIG. 7. (a) Upper-layer streamfunction (Sv) for the case with ice–ocean drag and ice pumping; (b) no sea ice. The difference between the case with ice and the case without ice for the upper-layer (c) streamfunction (Sv) and (d) thickness (m). The red line in (c) and (d) is the zero contour.

because the model applies the drag throughout the upper layer, while a more accurate representation of the vertical structure shows that the drag effects are really confined to the upper Ekman layer and have little effect on the deep halocline eddies (Meneghello et al. 2021). Larger values of C_i result in weaker eddies, a stronger mean circulation, and thus stronger ice pumping.

b. Model results

We present results from four model simulations. The first is a case with sea ice with the ice–ocean drag term but with no ice pumping. The impact of the pumping is then demonstrated by including the right-hand side term in (9). The overall impact of ice is shown by removing both the ice-pumping term and the ice–ocean drag term [the terms with C_i in (7)]. Finally, we repeat the ice-pumping calculation in which the ice thickness keeps the same pattern, but its amplitude oscillates in time with $\phi = 1$ in (12).

The mean upper-layer streamfunction for the case with ice–ocean drag but no ice pumping is shown in Fig. 6a. The maximum transport in the anticyclonic gyre is about 6 Sv ($1\ \mathrm{Sv} \equiv 10^6\ \mathrm{m^3\ s^{-1}}$), while that in the cyclonic gyre is about −3.5 Sv. The smaller transport in the cyclonic gyre results from the thinner upper layer, an asymmetry not included in quasigeostrophic dynamics. The upper-layer thickness varies from about 350 m in the anticyclonic gyre to 65 m in the cyclonic gyre. The velocity in the region between the thick upper layer and the thin upper layer is $O(5)\ \mathrm{cm\ s^{-1}}$.

The case with ice pumping produces a stronger anticyclonic gyre (6.8 Sv) and a weaker cyclonic gyre (−2.4 Sv), as shown in Fig. 6b. The pathway of the model Transpolar Drift Current is also shifted toward the cyclonic gyre. Taking the difference between Figs. 6b and 6a shows that the ice pumping produces a basin-scale anticyclonic circulation anomaly, centered at the pole, of magnitude 3.5 Sv. This is consistent with the circulation pattern and strength predicted by the theory in the previous section.[1] The upper-layer thickness reflects this anticyclonic circulation such that the halocline is deeper near the pole and shallower around the basin perimeter. The halocline is adiabatic in this model so this change in layer thickness integrates to zero over the basin.

Sea ice acts to stabilize the gyres due to the ice–ocean drag term (Meneghello et al. 2021). This is reflected by the case with no sea ice shown in Fig. 7b, where the anticyclonic gyre is only 4.3 Sv and the cyclonic gyre is −3.1 Sv. This is accompanied by a shallower halocline in the central and anticyclonic basin and a deeper halocline in the cyclonic basin.

The ice cover in the Arctic Ocean has a strong seasonal cycle. This is approximated here by setting $\phi = 1$ in (12). This reduces the mean ice thickness, and the ice cover slope, by a factor of 2. This results in no ice gradient, or pumping, during the model summer, although in reality there is an ice cover slope present north of Greenland all yearlong. The purpose of

[1] Keep in mind that the model and the theory have different patterns of surface stress.

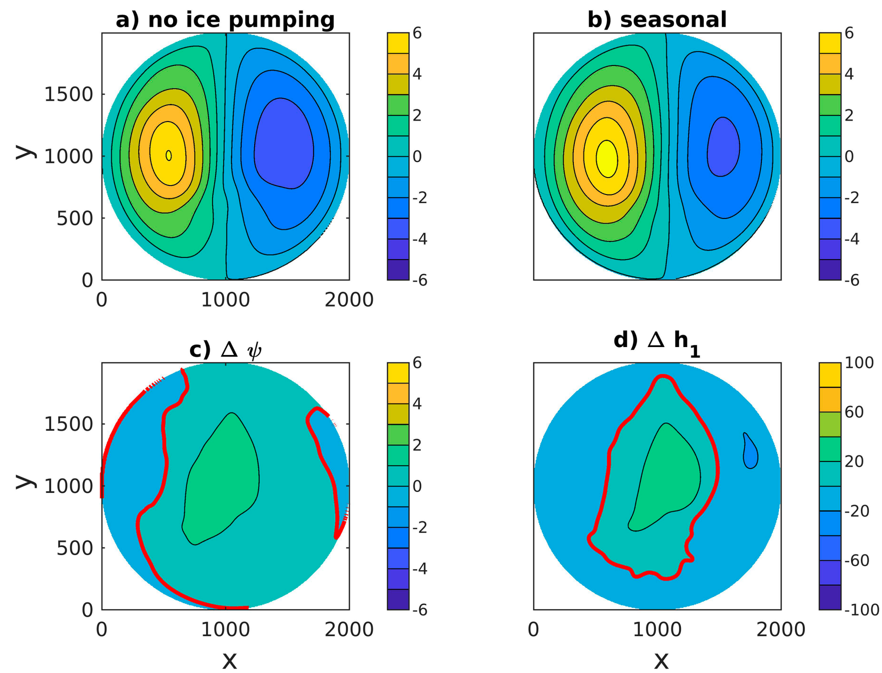

FIG. 8. Upper-layer streamfunction (Sv) for (a) the central case with ice–ocean drag and no ice pumping; (b) a seasonal cycle. The difference between the case without ice pumping and with a seasonal cycle in ice pumping for (c) streamfunction (Sv) and (d) thickness (m). The red line in (c) and (d) is the zero contour.

this calculation is to test whether the ice–ocean coupling is approximately linear in this parameter regime so that the influences of sea ice can be approximated by the annual-mean ice distribution. The time-mean streamfunction shows the same pattern of anomalous circulation compared to the case with no ice pumping, only reduced by a factor of 2 (Fig. 8). So we can expect that the basic mechanism demonstrated by these steady solutions will be found even in the presence of a strong seasonal cycle. In addition, there is a rapid, barotropic response to the varying ice thickness gradient such that the anomalous anticyclonic gyre spins up and down on the seasonal time scale with an amplitude of $O(1)$ Sv.

4. Discussion and conclusions

The sloping sea ice cover acts as an upside-down bathymetry, generating a vertical velocity, which we dub ice pumping, and steering the underlying circulation in a manner comparable to bottom topography. Our observational estimates (Fig. 2) suggest that the ice pumping influence on the large-scale circulation dynamical balance is, in the central Arctic, comparable to that of mesoscale eddies and of planetary vorticity advection. Our theoretical and numerical models show how small ice thickness gradients, on the order of a meter over a 1000 km, combined with mean surface currents of a few centimeters per second, are sufficient to generate an ice pumping that drives a substantial change in the large-scale circulation.

Crucially, the ice-pumping mechanism remains dynamically relevant even on the long time scales for which the deep circulation is typically assumed to be at rest, and classical topographic steering is therefore expected to play only a minor role away from the coast. This is particularly important given that the Arctic wind–driven circulation is largely confined to the upper 300 m, whereas most bathymetry outside the continental shelves lies deeper than 2000 m. We therefore propose that ice thickness needs to be considered in a conservation principle analogous to f/h in an ice-free ocean, in which h is set by ice thickness in addition to bathymetry, especially on long time scales.

Our analysis captures the main features of the Arctic circulation but remains idealized. A quantitative comparison with the observed circulation would require, at minimum, a more realistic distribution of Ekman pumping and possibly the inclusion of coastline geometry, straits, and bathymetry. Nonetheless, some general conclusions about how ice pumping can shift the Arctic circulation are robust across both the theory and the numerical model and can be stated with confidence. These are summarized in Fig. 9. As the ice thickness gradient increases from zero ($P = 0$) to 2 m over 1000 km ($P = 2$), the Transpolar Drift Current—marked by the streamline separating the anticyclonic and cyclonic gyres—and the centers of the two gyres—marked by dots—shift rightward toward the Eurasian coast. The current's outflow moves eastward by more than 500 km, potentially redirecting a larger fraction of the transport toward the East Greenland Current and out of the Arctic (not represented in our model), rather than toward the recirculating Beaufort Gyre or the Canadian Arctic Archipelago (Figs. 9a,c).

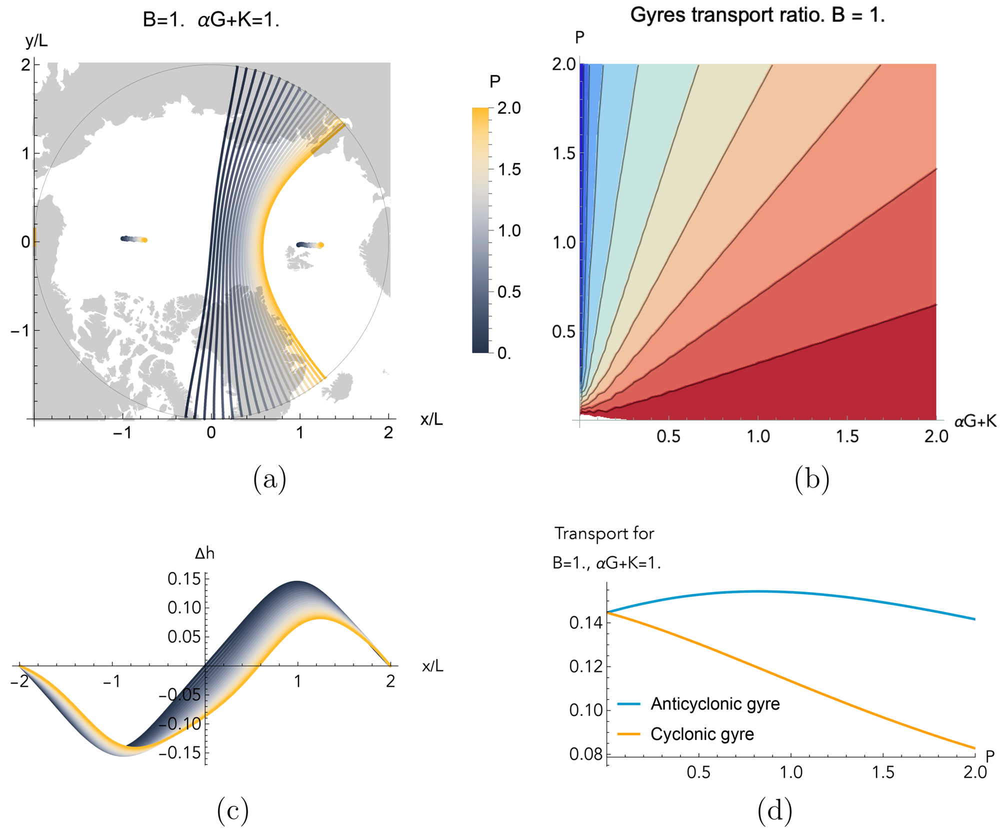

FIG. 9. Modulation of Arctic circulation by ice pumping. (a) The Transpolar Drift Current trajectory (lines) and the gyres' centers (points) as a function of the ice-pumping parameter P (color), overlaid on a map of the Arctic; (b) the ratio between the cyclonic and the anticyclonic gyres' transport, as a function of the ice-pumping parameter P and the governor/thickness-diffusion parameter $\alpha G + K$; (c) isopycnal depth anomaly along the line connecting the gyres centers, as a function of the ice-pumping parameter P; (d) the gyres' transport for $\alpha G + K = 1$ as a function of P. As the ice thickness increases, the Transpolar Drift Current trajectory and the gyre centers move toward the Eurasian coast, and the cyclonic gyre's transport is reduced.

Shifts in the Transpolar Drift Current are accompanied by changes in gyre transport. As the ice thickness gradient increases, the anticyclonic gyre grows in size, and the cyclonic gyre weakens, as shown in Fig. 9d. The ratio of the two gyres transports, $[\min(\tilde{h}) - \tilde{h}_b]/[\max(\tilde{h}) - \tilde{h}_b]$, where $\tilde{h}_b$ is the layer thickness at the Transpolar Drift (the same as at the boundary), is presented in Fig. 9b as a function of the ice-pumping strength P and the combined governor/eddy-flux parameter $\alpha G + K$. The circulations at the extremes of the parameter space are the ones shown in Fig. 4: the circulation at the origin (Fig. 4a), the symmetric circulation for large $\alpha G + K$ (Fig. 4b), and the single-gyre circulation for large P (Fig. 4c). The circulation for comparable P and $\alpha G + K$ is the one shown in Fig. 5b.

Our study focuses on the Arctic, but the theory developed here is sufficiently general to apply to other ice-covered oceans. Two candidate applications come to mind. The first is for the flow under ice shelves, as can be inferred by, e.g., the study of Little et al. (2008). Ice shelf thickness gradients, ranging from 0.5 to 1.5 m km^{-1}, are much larger than sea ice thickness gradients, while ocean currents are typically comparable. Ice pumping could play a dominant role in the circulation under ice shelves.

The second is oceans on icy moons such as Enceladus and Europa, where ice thickness gradients are much larger than in the Arctic, and current speeds may be comparable. For example, Enceladus exhibits sea ice thickness variations on the order of 10 km over characteristic length scales of about 100 km, corresponding to ice thickness gradients roughly 10^5 times larger than those on Earth (Čadek et al. 2016), while ocean currents are estimated to be on the order of centimeters per second (Soderlund 2019). In such environments, the Ekman pumping term would need to be replaced by an alternative source of potential vorticity. Nevertheless, the remainder of the theoretical framework is expected to remain applicable, and the large ice thickness gradients suggest that ice pumping may play an important dynamical role.

Acknowledgments. G. M. acknowledges support from the ANR program under Grant ANR-22-CPJ2-0063-01. M. A. S. was supported by NSF Grants OCE2241083 and OCE2420209.

The authors thank Joe Pedlosky for suggesting this ice–ocean interaction problem.

Data availability statement. The observational datasets used in this estimate are sea ice thickness from Ricker et al. (2017), sea ice concentration from Meier et al. (2024), sea ice velocity from Tschudi et al. (2019), dynamic ocean topography from Armitage et al. (2016, 2017), and geostrophic winds derived from atmospheric geopotential fields from Hersbach et al. (2023).

REFERENCES

Armitage, T. W. K., S. Bacon, A. L. Ridout, S. F. Thomas, Y. Aksenov, and D. J. Wingham, 2016: Arctic sea surface height variability and change from satellite radar altimetry and GRACE, 2003–2014. *J. Geophys. Res. Oceans*, **121**, 4303–4322, https://doi.org/10.1002/2015JC011579.

——, ——, ——, A. A. Petty, S. Wolbach, and M. Tsamados, 2017: Arctic Ocean surface geostrophic circulation 2003–2014. *Cryosphere*, **11**, 1767–1780, https://doi.org/10.5194/tc-11-1767-2017.

Čadek, O., and Coauthors, 2016: Enceladus's internal ocean and ice shell constrained from Cassini gravity, shape, and libration data. *Geophys. Res. Lett.*, **43**, 5653–5660, https://doi.org/10.1002/2016GL068634.

Cushman-Roisin, B., and J.-M. Beckers, 2010: Introduction to geophysical fluid dynamics. *Physical and Numerical Aspects*, B. Cushman-Roisin and J.-M. Beckers, Vol. 101. Academic Press, 786 pp., https://doi.org/10.1016/B978-0-12-088759-0.00022-5.

Davis, P. E. D., C. Lique, and H. L. Johnson, 2014: On the link between Arctic sea ice decline and the freshwater content of the Beaufort Gyre: Insights from a simple process model. *J. Phys. Oceanogr.*, **27**, 8170–8184, https://doi.org/10.1175/JCLI-D-14-00090.1.

Dewey, S., J. Morison, R. Kwok, S. Dickinson, D. Morison, and R. Andersen, 2018: Arctic ice-ocean coupling and gyre equilibration observed with remote sensing. *Geophys. Res. Lett.*, **45**, 1499–1508, https://doi.org/10.1002/2017GL076229.

Doddridge, E. W., G. Meneghello, J. Marshall, J. Scott, and C. Lique, 2019: A three-way balance in the Beaufort Gyre: The ice-ocean governor, wind stress, and eddy diffusivity. *J. Geophys. Res. Oceans*, **124**, 3107–3124, https://doi.org/10.1029/2018JC014897.

Hersbach, H., and Coauthors, 2023: ERA5 post-processed daily statistics on pressure levels from 1940 to present. Copernicus Climate Change Service (C3S) Climate Data Store (CDS), accessed 14 December 2021, https://doi.org/10.24381/cds.4991cf48.

Lique, C., H. L. Johnson, and P. E. D. Davis, 2015: On the interplay between the circulation in the surface and the intermediate layers of the Arctic Ocean. *J. Phys. Oceanogr.*, **45**, 1393–1409, https://doi.org/10.1175/JPO-D-14-0183.1.

Little, C. M., A. Gnanadesikan, and R. Hallberg, 2008: Large-scale oceanographic constraints on the distribution of melting and freezing under ice shelves. *J. Phys. Oceanogr.*, **38**, 2242–2255, https://doi.org/10.1175/2008JPO3928.1.

Manucharyan, G., and M. A. Spall, 2016: Wind-driven freshwater buildup and release in the Beaufort Gyre constrained by mesoscale eddies. *Geophys. Res. Lett.*, **43**, 273–282, https://doi.org/10.1002/2015GL065957.

Meier, W., F. Fetterer, A. Windnagel, J. S. Stewart, and T. Stafford, 2024: NOAA/NSIDC climate data record of passive microwave sea ice concentration, version 5. National Snow and Ice Data Center, accessed 21 November 2024, https://doi.org/10.7265/RJZB-PF78.

Meneghello, G., J. Marshall, S. T. Cole, and M.-L. Timmermans, 2017: Observational inferences of lateral eddy diffusivity in the halocline of the Beaufort Gyre. *Geophys. Res. Lett.*, **44**, 12 331–12 338, https://doi.org/10.1002/2017GL075126.

——, ——, J.-M. Campin, E. Doddridge, and M.-L. Timmermans, 2018a: The ice-ocean governor: Ice-ocean stress feedback limits Beaufort Gyre spin-up. *Geophys. Res. Lett.*, **45**, 11 293–11 299, https://doi.org/10.1029/2018GL080171.

——, ——, M.-L. Timmermans, and J. Scott, 2018b: Observations of seasonal upwelling and downwelling in the Beaufort Sea mediated by sea ice. *J. Phys. Oceanogr.*, **48**, 795–805, https://doi.org/10.1175/JPO-D-17-0188.1.

——, E. Doddridge, J. Marshall, J. Scott, and J.-M. Campin, 2020: Exploring the role of the "ice–ocean governor" and mesoscale eddies in the equilibration of the Beaufort Gyre: Lessons from observations. *J. Phys. Oceanogr.*, **50**, 269–277, https://doi.org/10.1175/JPO-D-18-0223.1.

——, J. Marshall, C. Lique, P. E. Isachsen, E. Doddridge, J.-M. Campin, H. Regan, and C. Talandier, 2021: Genesis and decay of mesoscale baroclinic eddies in the seasonally ice-covered interior Arctic Ocean. *J. Phys. Oceanogr.*, **51**, 115–129, https://doi.org/10.1175/JPO-D-20-0054.1.

Munk, W. H., 1950: On the wind-driven ocean circulation. *J. Meteor.*, **7**, 80–93, https://doi.org/10.1175/1520-0469(1950)007<0080:OTWDOC>2.0.CO;2.

Nilsson, J., J.-A. H. Kallmyr, and P. E. Isachsen, 2024: Topographic steering of the upper Arctic Ocean circulation by deep flows. *Tellus*, **76** (1), 206–226, https://doi.org/10.16993/tellusa.4072.

Nöst, O. A., and P. E. Isachsen, 2003: The large-scale time-mean ocean circulation in the Nordic Seas and Arctic Ocean estimated from simplified dynamics. *J. Mar. Res.*, **61**, 175–210.

Ricker, R., S. Hendricks, L. Kaleschke, X. Tian-Kunze, J. King, and C. Haas, 2017: A weekly Arctic sea-ice thickness data record from merged CryoSat-2 and SMOS satellite data. *Cryosphere*, **11**, 1607–1623, https://doi.org/10.5194/tc-11-1607-2017.

Smagorinsky, J., 1963: General circulation experiments with the primitive equations: I. The basic experiment. *Mon. Wea. Rev.*, **91**, 99–164, https://doi.org/10.1175/1520-0493(1963)091<0099:GCEWTP>2.3.CO;2.

Soderlund, K. M., 2019: Ocean dynamics of outer solar system satellites. *Geophys. Res. Lett.*, **46**, 8700–8710, https://doi.org/10.1029/2018GL081880.

Spall, M. A., 2019: Dynamics and thermodynamics of the mean transpolar drift and ice thickness in the Arctic Ocean. *J. Climate*, **32**, 8449–8463, https://doi.org/10.1175/JCLI-D-19-0252.1.

——, 2020: Potential vorticity dynamics of the Arctic halocline. *J. Phys. Oceanogr.*, **50**, 2491–2506, https://doi.org/10.1175/JPO-D-20-0056.1.

Sverdrup, H. U., 1947: Wind-driven currents in a baroclinic ocean; with application to the equatorial currents of the eastern Pacific. *Proc. Natl. Acad. Sci. USA*, **33**, 318–326, https://doi.org/10.1073/pnas.33.11.318.

Tschudi, M., W. N. Meier, J. S. Stewart, C. Fowler, and J. Maslanik, 2019: Polar pathfinder daily 25 km EASE-grid sea ice motion vectors, version 4. NASA National Snow and Ice Data Center Distributed Active Archive Center, accessed 9 July 2021, https://doi.org/10.5067/INAWUWO7QH7B.

Willmott, A. J., and M. Luneva, 2015: Steady, barotropic wind and boundary-driven circulation on a polar plane. *Geophys. Astrophys. Fluid Dyn.*, **109**, 216–233, https://doi.org/10.1080/03091929.2015.1050589.

Yang, J., A. Proshutinsky, and X. Lin, 2016: Dynamics of an idealized Beaufort Gyre: 1. The effect of a small beta and lack of western boundaries. *J. Geophys. Res. Oceans*, **121**, 1249–1261, https://doi.org/10.1002/2015JC011296.

Zhong, W., M. Steele, J. Zhang, and J. Zhao, 2018: Greater role of geostrophic currents in Ekman dynamics in the western Arctic Ocean as a mechanism for Beaufort Gyre stabilization. *J. Geophys. Res. Oceans*, **123**, 149–165, https://doi.org/10.1002/2017JC013282.